Permittivity analysis of weathered concrete in a bridge based on open-ended probe and impedance measurements

Benhui Fan, Frédéric Bosc, Yu Liu, Mathieu Le Feuvre, Cyrille Fauchard

▶ **To cite this version:**

Benhui Fan, Frédéric Bosc, Yu Liu, Mathieu Le Feuvre, Cyrille Fauchard. Permittivity analysis of weathered concrete in a bridge based on open-ended probe and impedance measurements. Construction and Building Materials, 2024, 429, pp.136354. 10.1016/j.conbuildmat.2024.136354 . hal-04568942

HAL Id: hal-04568942
https://hal.science/hal-04568942v1

Submitted on 6 May 2024

HAL is a multi-disciplinary open access archive for the deposit and dissemination of scientific research documents, whether they are published or not. The documents may come from teaching and research institutions in France or abroad, or from public or private research centers.

L'archive ouverte pluridisciplinaire **HAL**, est destinée au dépôt et à la diffusion de documents scientifiques de niveau recherche, publiés ou non, émanant des établissements d'enseignement et de recherche français ou étrangers, des laboratoires publics ou privés.

Permittivity Analysis of Weathered Concrete in a Bridge Based on Open-ended Probe and Impedance Measurements

Benhui Fan[1]*, Frédéric Bosc[1], Yu Liu[2], Mathieu Le Feuvre[1], Cyrille Fauchard[3]*

[1]Cerema, Research Team ENDSUM, 23 avenue Amiral Chauvin, 49136, Les Ponts de Cé, France

[2]State Key Laboratory of Powder Metallurgy, Powder Metallurgy Research Institute, Central South University, 410083 Changsha, PR China

[3]Cerema, Research Team ENDSUM, 10 chemin de la Poudrière, 76120, Le Grand-Quevilly, France

Corresponding: benhui.fan@cerema.fr ; cyrille.fauchard@cerema.fr

Abstract

Pathologies like corrosion of rebars or alkali aggregate reactions in a reinforced concrete (RC) bridge are usually accompanied by the existence of aqueous pore solutions with a high concentration of ions. The distribution of aqueous solutions in the concrete is inhomogeneous and depends on the RC's location in the bridge and complex climate factors. Frequency-dependent complex permittivity is sensitive to aqueous pore solutions because the high conductivity caused by charge carriers can result in a large imaginary part of the permittivity, much higher than that caused by water. In this study, we used a non-destructive open-ended probe to measure the complex permittivity of the RC in a bridge's pillar with different levels of pathologies. By measuring the impedance of core samples with various controlled water volumetric fractions in the laboratory, the water effect on the evolution of the loss tangent (the ratio between the imaginary part of the permittivity and the real part) can be calibrated. Comparing the loss tangent in the bridge with that of the core samples treated by water, we can map the areas with a high density of aqueous pore solution and cracks, and estimate the unhealthy area with partial damage in the pillar by an effective and non-destructive diagnosis.

Keywords

complex permittivity, loss tangent, reinforced concrete, open-ended probe, impedance analysis

Introduction

Water content is an important factor in evaluating the service life of reinforced concrete (RC) since some pathologies like corrosion, carbonation, and alkali aggregate reactions (AAR) are highly related to moisture [1-3]. The dielectric constant has been viewed as an indicator to estimate water content in RC because water has a much higher relative dielectric constant (~80) than that of dry concrete (~5). The application of electrical and electromagnetic geophysical methods for permittivity analysis in a large frequency domain (from 0.1 Hz to several GHz) has been an important issue in the structural health monitoring of RC based on the estimation of its water content [4-6].

Empirical models have been developed to calibrate the water content based on the measured complex permittivity in the concrete [7-9]. However, the ion effects are not well described in these models where the volumetric fraction of water is the only parameter for the calculation. In some real construction structures like bridges, the health of concrete is not simply associated with the water content but highly with the saline solutions [10, 11]. Moreover, the distribution of these aqueous pore solutions is inhomogeneous. The areas with a highly concentrated saline solution usually suffer grave partial damage. Thus, the development of permittivity analysis with the consideration of ion effects can be quite useful in evaluating the durability of RC.

Some research works have indicated that brine-saturated concrete has higher complex permittivity, especially the imaginary part of the permittivity than that of water-saturated concrete due to the high conductivity. However, these permittivity measurements are limited to newly made concrete samples in the laboratory [12, 13]. The weathered concrete of a bridge with long-term service has a much more complicated structure than that of newly-made concrete. Hence, on-site permittivity analysis of weathered concrete in a bridge can provide more representative results but these topics have not been widely reported in the literature.

On-site permittivity testing needs a large-scale investigation. Currently, there are two main methods for conducting non-intrusive permittivity measurements: a capacitive probe providing the dielectric constant at the resonant frequency [13, 14], and an open-ended probe providing the frequency-dependent permittivity in a wide band [15-18]. Compared with the mono-frequency test by the capacitive probe, the frequency-dependent test by the open-ended probe can provide rich information on the dielectric dissipation [19-20], which is useful for studying the polarizations caused by the discontinuities and aqueous pore solutions in the concrete. Therefore, in this study, an on-site permittivity measurement by an

open-ended probe in a bridge's pillar has been carried out to evaluate the dispersion of the aqueous pore solutions in weathered concrete with different levels of pathologies.

This work is divided into three parts: the first one is the presentation of the on-site test. Two faces (the east and west ones) of a bridge's pillar #12 were selected, where the various densities of cracks could be observed that should be caused by different levels of pathologies like rebar corrosion and AAR. This could provide an ideal site to study the distribution of aqueous pore solution in the concrete. Secondly, to distinguish the area that has been damaged gravely by saline solutions from the area with less saline solution, we did a calibration test, in which the core samples were only treated by water in the laboratory. The complex permittivity of the samples with different water contents (0-7 %) created by isothermal treatments was studied by an impedance analyzer from 1 Hz to 10^6 Hz. Applying a general dielectric relaxation model [21], the complex permittivity at gigahertz frequency can be obtained to represent the water effect. In the third part, we compare the complex permittivity of the core samples to the on-site results. As the core samples have been treated with water, their loss tangent (the ratio between the imaginary part of the permittivity and the real part) is quite different from that of the weathered concrete caused by aqueous pore solutions. This comparison can help to map the unhealthy areas with different levels of damage.

On-site permittivity test for two faces of Pillar #12 by an open-ended probe

The tested bridge was built in 1989. The cement for the constitution was Portland cement CEM II/A-LL 42.5, and the aggregates were gneiss (Pontraux quarry) with different grain size distributions (5/11, 10/14, 14/20).

The test was performed on August 8th, 2023, a fine day at 16-22°C. We chose two faces of Pillar #12, the east and the west faces as presented in Figures 1 (a) and (b), because the two faces have the same reinforcement structure (19 vertical rebars with an interval of 0.224 m; 11 horizontal rebars with an interval of 0.3 m), but do not have a similar crack density on the surface. To reduce the potential increase caused by the rebar's conductivity on the complex permittivity, before the measurement, a ground penetrating radar (GPR, a GSSI StructureScan MiniXT at 2.7 GHz frequency) was used to find the position of the rebars. Then based on the positions of the hyperboles in the radargram (also known as B-scan, as presented in the lower left parts of Figures 1 (c) and (d)), we traced the rebar's positions in red solid lines on the wall and marked them in dashed black lines in the diagram. The points for the permittivity test were in the center of the grid, as indicated by the yellow crosses in the diagram.

(a)

(b)

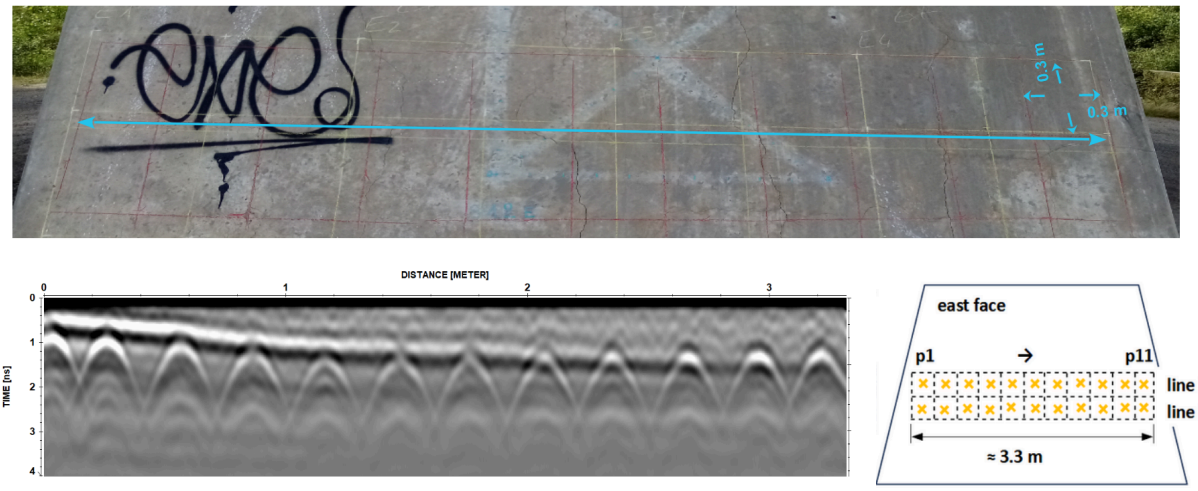
0.3 m
0.3 m

DISTANCE [METER]
0
1
2
3
TIME [ns]
0
1
2
3
4

east face
p1
p11
line 1
line 2
≈ 3.3 m

(c)

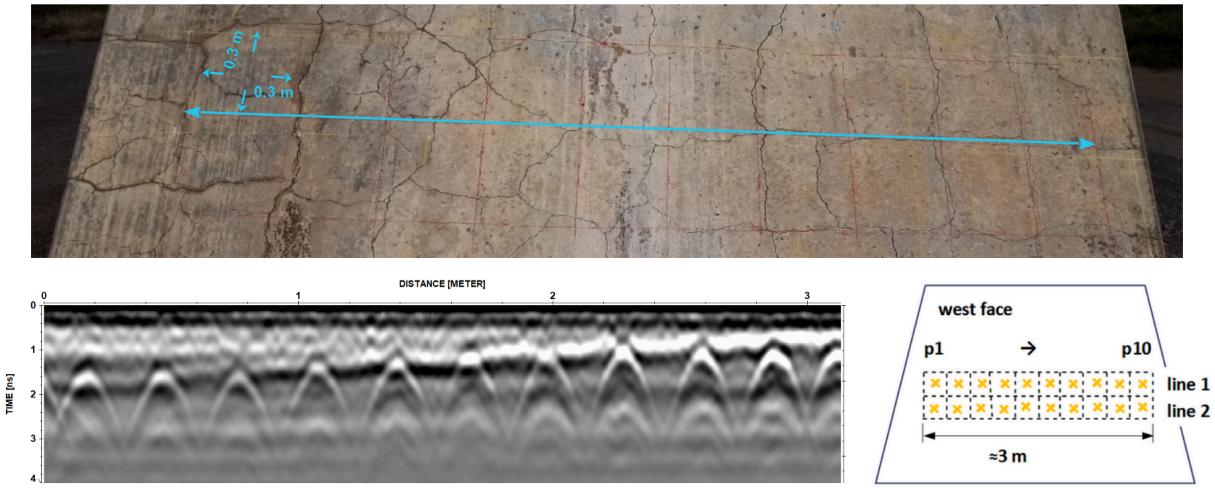

(d)

Figure 1 Pillar #12 for the test: (a) for the east face and (b) for the west face; Photo of the tested area in each face (above); radargram (B-scan) by GPR along a light blue line on the photo (lower left); diagram of the tested points (in yellow): (c) for the east face and (d) for the west face

The coaxial probe used in this test has an inner diameter of 32.2 mm and an outer diameter of 75 mm as presented in Figure 2 (a). Its characteristic impedance (Z_0) is 50 Ω. The capacitance method was used to calculate the dielectric permittivity based on the tested complex reflection parameter (s11). The calibration for the probe was done by the tests of an open circuit, a short circuit, and a test on Teflon [22, 23]. The electromagnetic source was generated by a reflectometer (R60) from 1 MHz to 1.6 GHz. We take the measured reflection S-parameter (s11) on the east face as an example in Figure 2 (b), to explain the cut-off frequency. It can be found that the amplitudes of s11 in both real and imaginary parts are reduced when the frequency is over 0.5 GHz. This reduction is related to the electromagnetic properties of the medium and the geometry of the open-end probe. The frequency when s11 starts to decrease is known as the cut-off frequency. Besides the observation of the reduction of amplitude, the cut-off frequency can also be calculated by:

$$f_{cut-off}\ (in\ MHz) = \frac{20}{(b-a)\sqrt{\varepsilon_r}}$$

where a (in mm) and b (in mm) are the inner and outer radii of the coaxial probe, and ε_r is the dielectric constant of the tested medium. If using 5 as the dielectric constant reference of dry concrete, the $f_{cut\text{-}off}$ is

calculated as 430 MHz. Thus, the frequency domain for the analysis is cut at 0.4 GHz. The penetration depth of the probe is related to its outer radius (b). In our case, the penetration depth is around 4 cm.

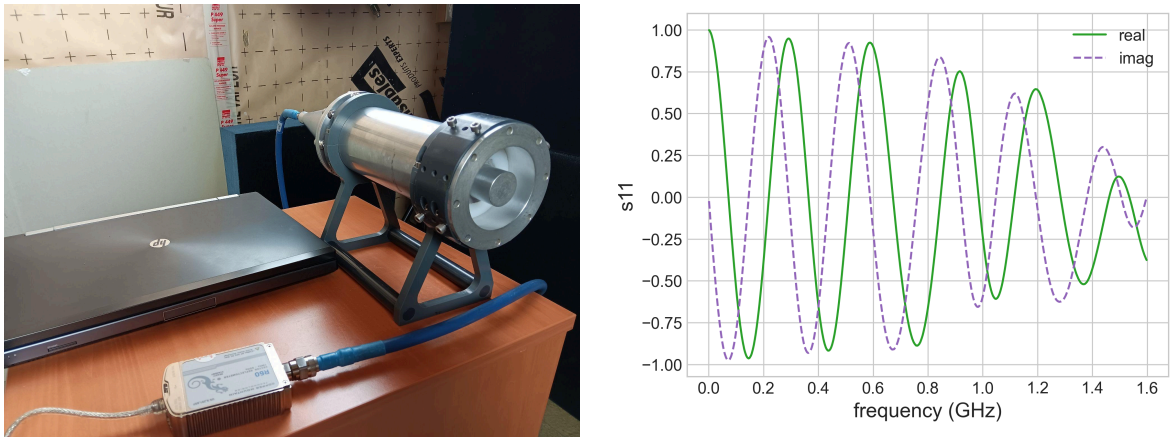

(a) (b)

Figure 2 (a) Photo of the open-ended probe and the EM generator R60. (b) Frequency-dependent s11 from 1MHz to 1.6 GHz: the green solid line for the real part and the violet dash line for the imaginary part.

Frequency-dependent complex permittivity of the east and the west faces are presented in Figures 3 and 4. The complex permittivity of the points is stable in the tested frequency range. In the east face, most of the points on the two lines have similar permittivity, except p5 and p7 on line 1, and p4, p6, and p7 on line 2 with lower values. The reduction of permittivity in these points on the east face should be associated with the existence of the crack on the surface. In contrast, the complex permittivity on the two lines of the west face is more frequency-dependent, with higher values in both real and imaginary parts than those of the east face. The difference in the complex permittivity between the east and west faces cannot be simply explained by the water content as mentioned before, because the measurement was conducted under the same weather condition.

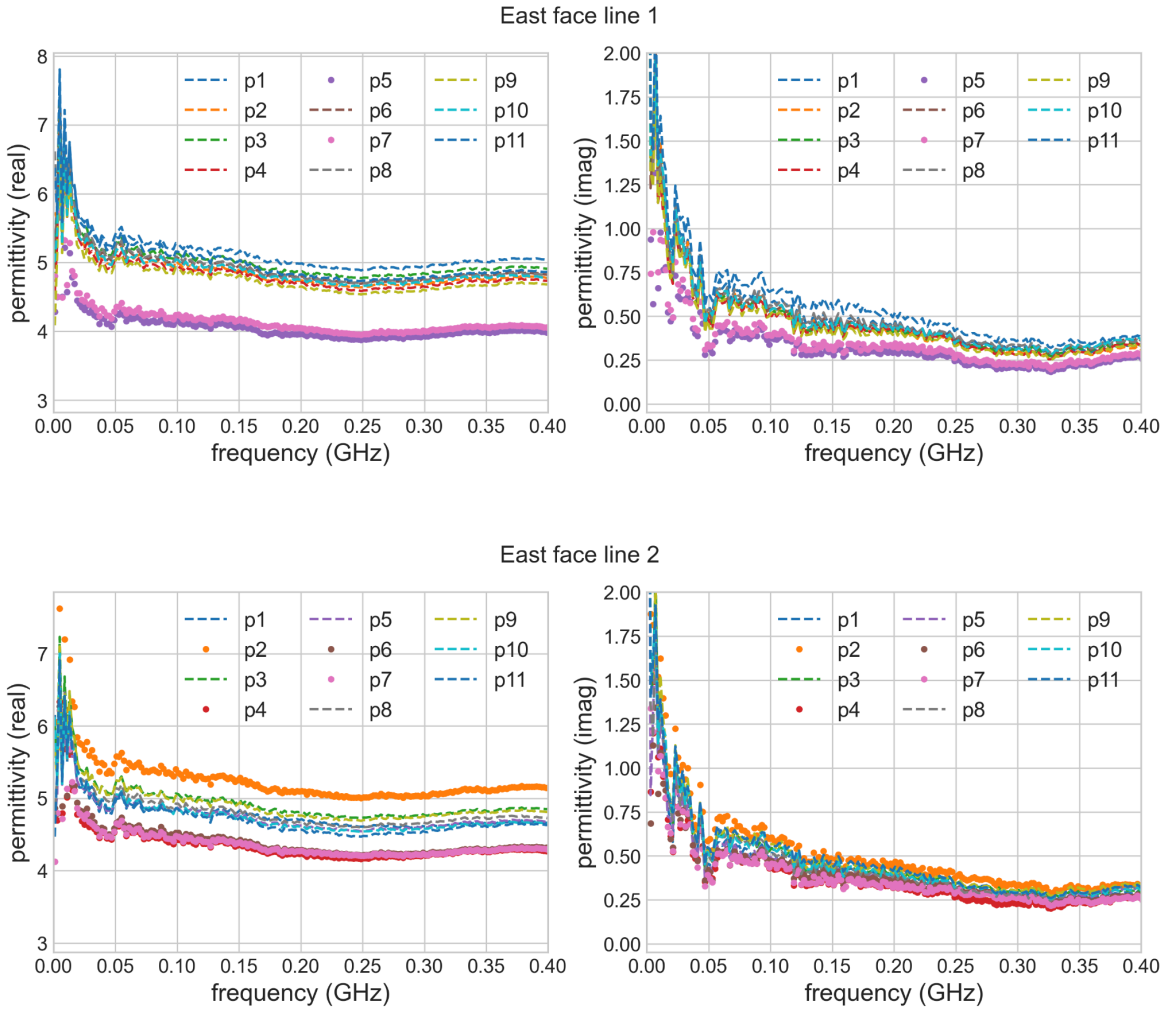

Figure 3 Frequency-dependent complex permittivity for two lines on the east face.

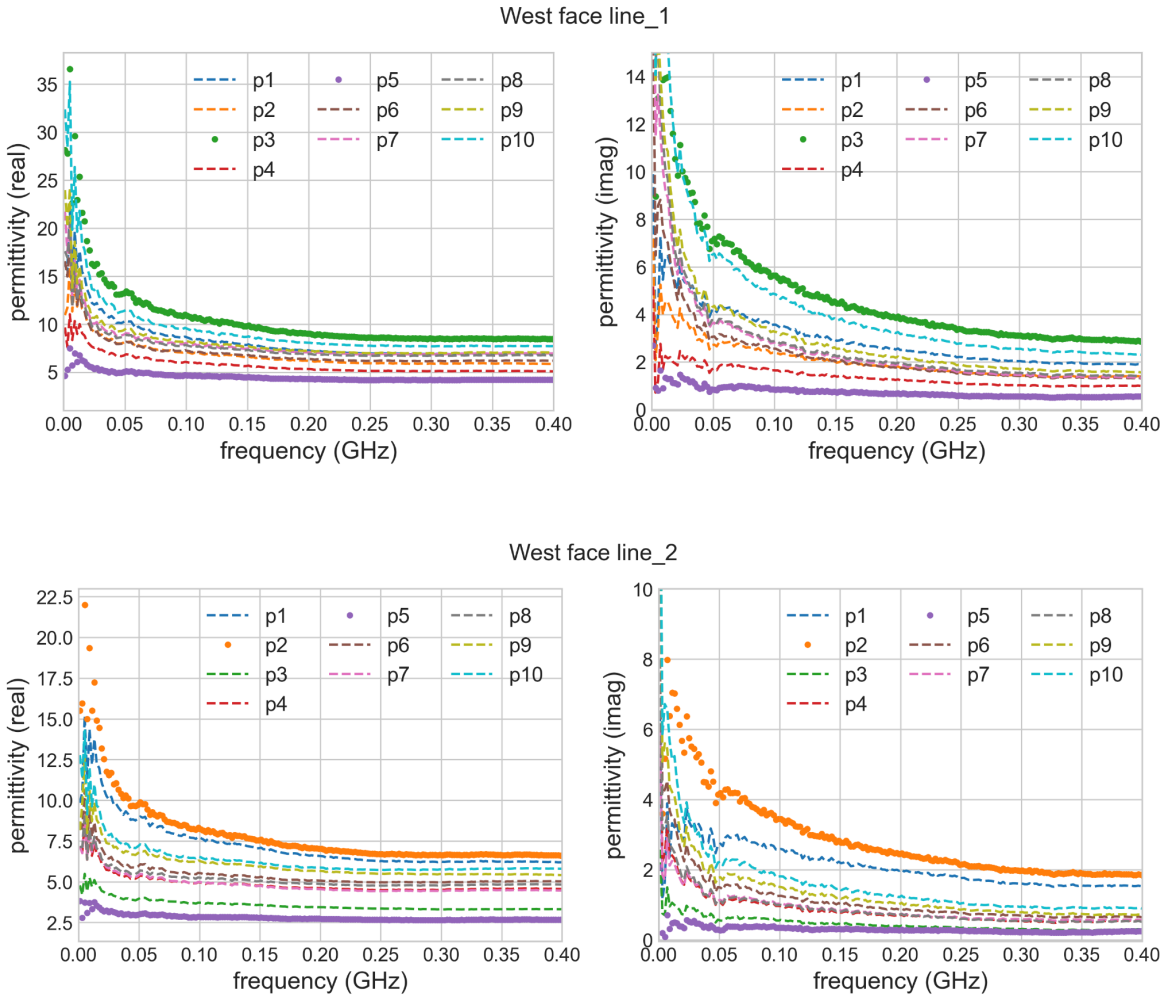

Figure 4 Frequency-dependent complex permittivity for two lines on the west face.

It is known that weathered concrete suffers from pathologies such as rebar corrosion, carbonation, AAR, etc., where the content of ions is usually higher than that of relatively healthy concrete. Since the bridge was built more than 30 years ago, we can see the obvious spread of the cracks along the framework on both the east and west faces as shown in the photos of Figure 1. Several reasons can be associated with this development of the cracks based on the position of the rebars and one of them is related to the volume's expansion of the corrosion products, known as the iron oxides[24]. However, the damage level between the east and west faces is different, as inferred by the different densities and development of cracks on the two faces in the photos: the growth of cracks on the west face is much higher than that of

the east face. Then, it is possible to associate the high dielectric permittivity of the west face with the high-level corrosion of the reinforcement.

The influence of corrosion on the complex permittivity of concrete can come from two possible parts: the corrosion products and the existence of aqueous pore solutions. On one hand, the corrosion products are mainly composed of iron oxides, but neither of them has a large dielectric contrast compared to the concrete [25]: magnetite ($FeO.Fe_2O_3$): $\varepsilon_r' = 5\text{-}6$, $\varepsilon_r'' = 0.15\text{-}0.22$; goethite (α-FeOOH). $\varepsilon_r' = 3\text{-}3.5$, $\varepsilon_r'' = 0.15\text{-}0.2$; maghemite ($\gamma\text{-}Fe_2O_3$): $\varepsilon_r' = \sim3$, $\varepsilon_r'' = \sim0.1$; hematite ($\alpha\text{-}Fe_2O_3$): $\varepsilon_r' = 2$, $\varepsilon_r'' = 0.05$. Thus, the contribution of corrosion products to the increase of the concrete's dielectric permittivity is less visible.

On the other hand, the effects of aqueous pore solutions are much more obvious. It is known that corrosion is generally accelerated by the marine atmosphere rich in chloride or the urban atmosphere rich in carbonate. The effect of these ions on the dielectric permittivity is usually accompanied by water since their movements need a moist medium. Dérobert et al [12] tested the dielectric permittivities of newly made concrete samples treated with freshwater and brine (NaCl solution, 30g/L, equal to that of the seawater) in the saturated and dried states. In their study, the complex permittivities of dried concrete samples treated by freshwater and brine did not present obvious differences: from 50 MHz to 400 MHz, for the water-treated concrete: $\varepsilon_r' = 4.95\text{-}5.00$, $\varepsilon_r'' = \sim0.06\text{-}0.10$; for the brine-treated concrete: $\varepsilon_r' = 4.90\text{-}4.95$, $\varepsilon_r'' = \sim0.04\text{-}0.08$. In contrast, when in a saturated state, for the water-treated concrete: $\varepsilon_r' = 7.5\text{-}9.0$, $\varepsilon_r'' = \sim1\text{-}4$; for brine-treated concrete: $\varepsilon_r' = 8\text{-}11.5$, $\varepsilon_r'' = \sim3\text{-}9$. The imaginary permittivity of the saturated brine-treated concrete nearly doubled that of the saturated water-treated concrete.

If we compare their reported results with our tests on the east and west faces of the pillar, some points on the west face such as p3 and p10 have similar complex permittivity as the brine-treated saturated concrete but the complex permittivity of the east face is more or less similar to the water-treated concrete. In real environments, the concrete will never be in a saturated state. Moreover, brine-treated concrete cannot well represent the weathered concrete. To analyze the dielectric difference between the east and the west faces, we use the core samples taken from the same bridge for the impedance analysis. In the laboratory, the weathered concrete with different levels of corrosion is hard to repeat; whereas creating core samples with different water contents can be easier to control. Comparing the on-site permittivity with the ones of the core samples treated by water can help to distinguish the area with water from the one with aqueous pore solutions.

Impedance analysis for the core samples by the laboratory

In 2005, some core samples (φ = 8 cm, length =15 cm) were taken out from Pillars S10-S12. The density, porosity, and size distribution of the pores were tested and written in a technical report by Dr. Villain [26]. The evaluation consumed several core samples at that moment, but the rest of them were well stored in the laboratory till now.

In this study, we took one of the remaining core samples without visible rust for the dielectric analysis by an impedance analyzer (Solartron Materials LabXM) to study the water influence. The frequency domain for the measurement was from 1 Hz to 10^6 Hz. The calculation of the dielectric permittivity was based on the tested complex impedances and the parallel plate capacitor model [27]. The sample needed to be cut into disc shape to adapt to the geometry requirement of the testing device. Thus, we sliced the core sample into 15 discs. Each one was with a thickness range from 8 to 9 mm, as presented in Figure 5 (a). Since the size distribution of the aggregates in the concrete was extensive, considering the heterogeneity of the sample and the thickness limit that the sample holder can measure, a large ring low electrode (lo-electrode) with an inner diameter of 4 cm presented in Figure 5 (b) was used for the measurement. Three tests in the different regions of each piece were conducted to get an average value. The dielectric measurements were done directly without metallization.

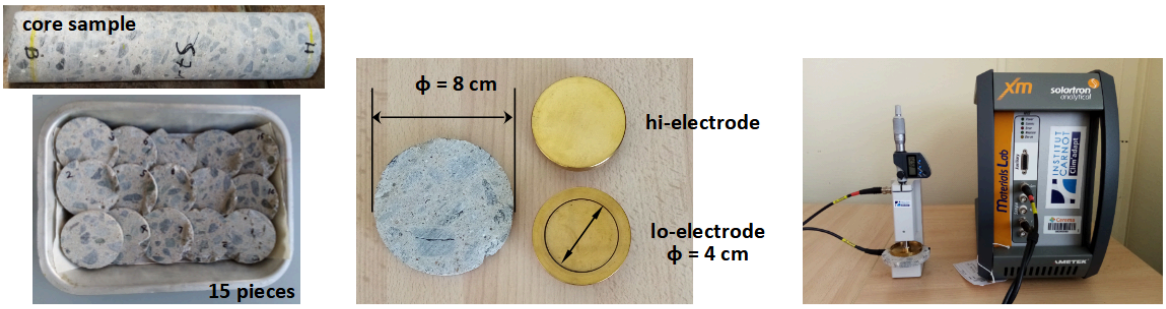

Figure 5 Tested samples (a), applied ring electrodes (b) and impedance analyzer (c)

The slicing process introduced water into the samples, which created an unsaturated state. We used isothermal treatments at different temperatures (at 50°C, 80°C, and 110°C) to remove the remaining water step by step. After each treatment, all the pieces were cooled naturally at 20°C to measure their

mass and calculate the water weight loss. Then the dielectric characterization was conducted at 20°C to follow the evolution of the dielectric permittivity caused by the loss of water.

Since the bridge was built in 1989 and the core samples were taken out in 2005, the core samples used in this test are not newly-made concrete. The dielectric change caused by the formation of C-S-H was not considered in this study [28, 29]. Furthermore, as we have mentioned, in 2005, the structural parameters of some core samples were tested by gammadensimetry, mercury intrusion porosimeter (MIP), and thermogravimetric analysis (TGA) by Dr. Villain [26]. According to the TGA in her report, from 20°C to 900 °C with a rising temperature speed of 10°C/min, except for the weight loss (around 2.2%) caused by the free water at 100°C, there is no other weight loss before 400°C. Therefore, we believe that the isothermal treatments at 50°C, 80°C, and 110°C just removed the free water in the concrete (also known as the capillary water in the macropores [1]).

Considering that the sample after 110°C treatment should be well dried, the free water volumetric fraction (θ) and the saturation (Sr) of each piece after the isothermal treatments can be calculated by the following equations, and the results are presented in Figure 6.

$$m_{i\ (water)} = m_{i\ (piece)} - m_{110°C\ (piece)}$$

$$\theta = \frac{m_{i\ (water)}}{V_{110°C\ (piece)}}$$

$$V_{110°C\ (piece)} = m_{110°C\ (piece)} * \rho_{dried\ sample}$$

$$Sr = \frac{m_{i\ (water)}}{V_{air}}$$

$$V_{air} = V_{110°C\ (piece)} * \varphi \quad V_{air} = V_{110°C\ (piece)} * \varphi$$

where $m_{110°C\ (piece)}$ is the weight after the treatment at 110°C; $m_{i\ (piece)}$ is the weight of the sample after each isothermal treatment (i = 20, 50, and 80°C); $m_{i\ (water)}$ is the weight of the remaining free water; $V_{110°C\ (piece)}$ is the volume after the treatment at 110°C, which can be calculated by the density of dried core samples (average value = 2.2 ± 0.1 kg/dm^3). The calculation of saturation (Sr) is based on the porosity (φ) of the core samples derived from MIP (average value = 16 ± 1 %).

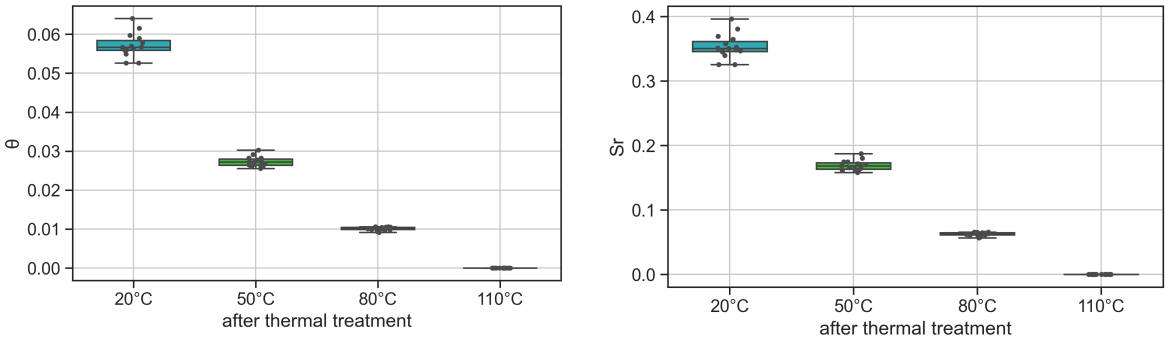

(a) (b)

Figure 6 Volumetric fraction of water (θ) and saturation (Sr) of the 15 pieces after isothermal treatments at different temperatures step by step

Frequency-dependent complex permittivities of 15 pieces were measured, and we use a bode plot of Piece #4 in Figure 7 (a) as an example to illustrate the analysis, where the real and imaginary parts, as well as the loss tangent, are plotted as a function of frequency. The complex permittivity of Piece #4 changes regularly after the isothermal treatments: both the real and imaginary parts gradually decrease as the treatment temperature increases. Meanwhile, the frequency peak in the loss tangent graph shifts from high to low frequencies. As shown in Figure 6, θ and Sr gradually decrease after each treatment. The shift of the frequency peak should be related to the free water content in the sample. Moreover, if we compare the evolution of the real part of permittivity, we can find that the 20°C curve has a plateau, but the plateau of the 50°C curve starts to disappear in the tested frequency domain. In the 80°C and 110°C curves, we no longer see the plateau. The shift of the loss tangent peak, the disappearance of plateaus in the real part, and the reduced value of both real and imaginary parts after the isothermal treatments can be explained by the modified polarization mechanisms proposed by A. Revil [4].

As illustrated in Figure 7 (b), in the frequency range from 10^{-3} Hz to10^{9} Hz, there are three polarization mechanisms: from low to high frequencies, they are the induction polarization (also known as the α polarization), the Maxwell-Wagner polarization (also known as the β polarization) and the dipolar polarization (also known as γ polarization), respectively. The α polarization plays a dominant role below 10^{4} Hz in a very broad frequency range. The β polarization follows between 10^{3} Hz to 10^{8} Hz. The γ polarization concerning water molecules passes gigahertz frequency. The frequency range of the impedance analyzer, as presented in the polarization diagram, covers the α and β polarizations.

The mechanism of α polarization is caused by the migration of the charge carriers that can usually be modeled by an electrical double layer [4, 21, 27]: in a porous medium, free water creates the electrical double layer between solid and air, where electromigration and accumulation/depletion of charge carriers occur and arouse α polarization. Meanwhile, this migration of the charge carriers can simultaneously increase the electrical conductivity (σ_{DC}). In our case, the visible increase of both real and imaginary dielectric permittivities at low frequency for the 20°C curve is caused by the strong α polarization and high σ_{DC}. Differently from α polarization, β polarization is the migration of charges at solid-solid discontinuities in the interfacial regions. Whenever the sample is dried or wet, β polarization always occurs because of the concrete's heterogeneity. This is why we can see one plateau in the dielectric real part of the 20°C curve, resulting from the combination of the two polarizations in the unsaturated concrete. After 50°C treatment, the free water starts to be removed, which reduces the volume of electrical double layers between solid and air and leads to longer relaxation time for charge carriers in the electrical double layers. Consequently, the loss tangent peaks of the 50°C curve shift to a lower frequency, and the plateau in the real part starts to disappear. After being treated at 80 °C and 110 °C, the free water in the macropores of the sample is largely removed, but the confined water in micro or mesopores cannot be thoroughly removed at these two temperatures. Thus, the α polarization still exists in the 80°C and 110°C curves, but the peaks shift to a much lower frequency that is not covered in this test. This is why neither of the two curves has a visible plateau in the real curves. Meanwhile, the values of σ_{DC} in these two curves are largely reduced due to the removal of the free water, which causes the obvious decrease in both real and imaginary dielectric permittivities. Although the peak of the α polarization shifts to a much lower frequency after the treatments at 80°C and 110°C, the β polarization always exists and becomes the main contributor to the complex permittivity and keeps a frequency-dependent characteristic.

This example of Piece #4 is not a special case, since the same phenomenon has been observed for the 15 pieces as presented in a statistical plot in Figure 8 (a): the higher the θ in the sample, the higher the frequency of the tangent peak. Hence, to conclude, the shift of the frequency after the different isothermal treatments is caused by the synergetic effects of the α and β polarizations. The removal of free water will shift the α polarization to a lower frequency until it is invisible in the tested range.

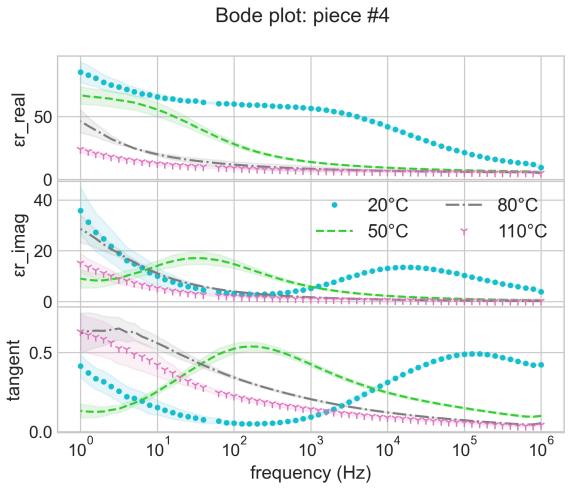

(a)

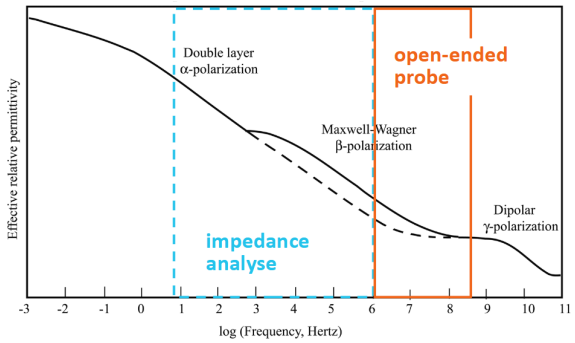

(b)

Figure 7 (a) Frequency-dependent dielectric properties (real, imaginary, and loss tangent) for Piece 4; (b) Representation of the three types of polarization proposed by A. Revil [4], and frequency domains of the two tests in this work: impedance analysis in a dahs grid and open-ended probe in a solid one.

Back to the representation of the three polarizations illustrated in Figure 7 (b), the polarization caused by water is γ occurring at gigahertz range, which is after α and β in the polarization curve. Thus, the tested data from 1 Hz to 10^6 Hz can be used to deduce the dielectric permittivity at high frequencies to discuss the water influence on the dielectric constant. A generalized dielectric relaxation model (GDR) [21] is used to fit the measured dielectric results:

$$\varepsilon^*_{r,eff} - \varepsilon_\infty = \sum_{k=1}^{N} \frac{\Delta\varepsilon_k}{(\omega j\tau_k)^{a_k} + (\omega j\tau_k)^{b_k}} - j\frac{\sigma_{DC}}{\omega\varepsilon_0}$$

where ε_∞ is the instantaneous dielectric constants; ω is the angular frequency, which is equal to 2πf; $\Delta\varepsilon_k$ and τ_k are the relaxation strength and time with the stretching exponents (a_k and b_k) in the k^{th} process. As mentioned before, the α and β polarizations are associated with the tested domain, then the two relaxation times (τ_α and τ_β) are used for the data fitting. The fitting process was done by the Gauss-Newton algorithm in the curve fit function of the Python Scipy Optimize package. The parameters for the fitting are listed in Table 1 (supporting information). Mean squared error (MSE) is used to

evaluate the fitting, where y_i^{test} is the i^{th} observed value, y_i^{model} is the corresponding predicted value for y_i^{test}, and n is the number of observations.

$$MSE = \frac{1}{N}\sum_{i=1}^{N}(y_i^{model} - y_i^{test})^2$$

Using the GDR model, we can obtain high-frequency permittivity, ε_∞. The influence of free water on the permittivity of the core samples will be analyzed by the fitted permittivity.

Generally, a third-order polynomial equation proposed by Topp et al. [30] is commonly used to relate the water content and the gigahertz dielectric constant of unsaturated soil. For concrete, the relation between water content and dielectric constant can be fitted by a linear equation. Villain et al [13] reported linear equations for θ and ε_∞ fitted a relaxation model based on tested dielectric permittivity, and the obtained linear models had high performance. They found that the parameters used in the linear model depend on the constituents of aggregates and porosity. In their study, they prepared concrete samples with 4 porosities and two types of aggregates (silico-calcareous or siliceous). We compare our fitting results to the two models in their study: one prepared by siliceous aggregates with a porosity of 15%, and the other by silico-calcareous aggregates with a porosity of 16%. As presented in Figure 8 (b), it can be found that the GDR fitted ε_∞ is well correlated to the θ. Meanwhile, most of the results in our tests fall in the region limited by the two margins proposed by the models in Villain's work. As mentioned before, different from the newly made concrete, the core samples used in this study are weathered concrete taken from a bridge after more than 15 years of service (1989-2005). Although the parameters in the linear equation of ε_∞ and θ obtained by fitting are not the same as the newly made concrete in their study, we believe the combination of the impedance test and the application of the GDR model can provide a permittivity reference for the effect of water. The objective of this study is not limited to discussing the water effect on the core samples but to distinguishing the damaged area from the relatively healthy one due to the aqueous pore solutions. Moreover, the imaginary part of the permittivity is extremely important for the analysis as mentioned before, then we will further use GDR to fit the complex permittivity at gigahertz for both core samples and on-site data to map the area with aqueous pore solutions.

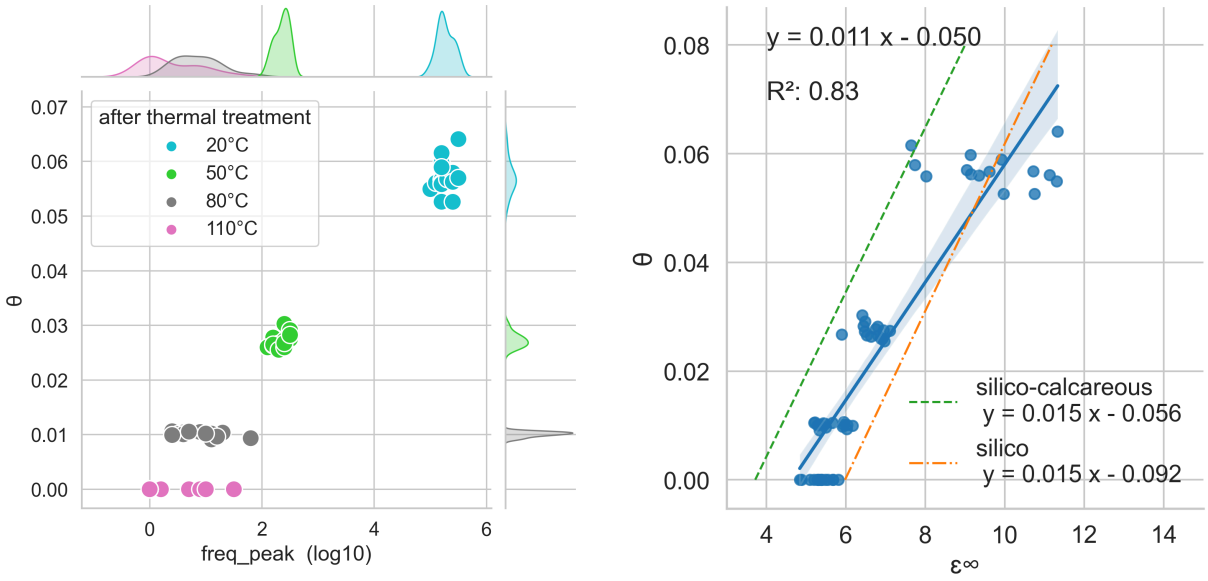

(a) (b)

Figure 8 (a) shift of frequency peak in decimal logarithm graph after different isothermal treatments; (b) linear fitting between the water volumetric fractions (θ) and the instantaneous dielectric constants (ε_∞) obtained by a generalized dielectric relaxation model (GDR). The dash lines are the models proposed by Villain et al. [13])

Comparison and discussion

Back to the on-site pillar data tested by the open-ended probe, as illustrated in the representative diagram in Figure 7 (b), the permittivity from 1 MHz to 400 MHz is also affected by α and β polarizations as the impedance analysis from 1 Hz to 1 MHz. Thus, two relaxation times (τ_α and τ_β) will be used to fit the real and imaginary parts of the tested points. The fitting results are listed in Table 2 in supporting information.

The ε_r' and ε_r'' fitted at 1 GHz by GDR for the east and west faces and the core sample are plotted in Figure 9 (a). We can find that the fitted complex permittivity of the points on the east face is closer to those of the core samples after the isothermal treatments, where the permittivity evolution is largely related to water content. However, most of the points on the west face are far away from the results of the core samples. The comparison of the complex permittivity infers much higher ion contents in the

concrete of the west face than that of the east face. If asking for a possible reason for the high-level ion contents in the west face, it is too complicated and far away from the objective of this work. A scenario may come from climate factors and the pillar's position. Checking the regional climate report, we can find a wind rose prepared based on the statistical data in 30 years in Figure 9 (b). The wind rose gives a succinct view of how wind speed and direction are distributed in that region. For the bridge, the southwest wind from the Atlantic makes the west face of the pillar more exposed to wet air, which increases the contents of aqueous pore solutions in the west face, which accelerates the pathologies of RC.

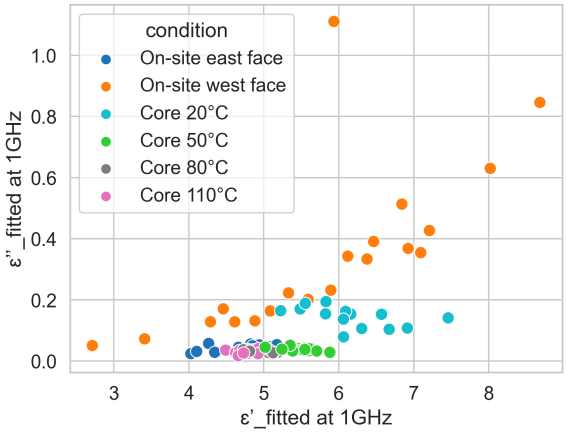

(a)

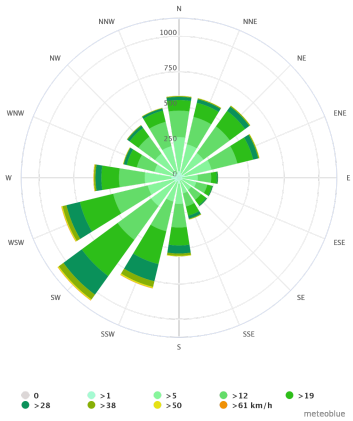

(b)

Figure 9 (a) values of real and imaginary parts at 1 GHz for the east and the west faces, and the core samples based on the experimental data fitted by GDR; (b) wind rose from a report of simulation of historical climate and weather data: https://www.meteoblue.com/fr/meteo/historyclimate/climatemodelled/nantes_france_2990969

Additionally, if we check the photos in Figure 1, we can see cracks on both faces. The influence of the cracks cannot simply be explained as a reduction of the dielectric constant because the bridge is never dry. The development of the cracks makes the concrete absorb the wet air more easily, which can sometimes increase the complex permittivity. This is also the reason why we find more obvious cracks on the west face than on the east face as shown in the photos, but the complex permittivity of the west face is much higher. Hence, we will use loss tangent as an indicator to compare the health of the concrete in

the two faces because the loss tangent contains both the imaginary part and real part of the complex permittivity.

We plot the value of tangent at 1 GHz related to the position in Figure 10. Meanwhile, the loss tangent of core samples after the different isothermal treatments is also plotted. The value of tangent is also known as dielectric loss [31]. When the value of the loss is high, it can be thought that the imaginary part is with a high value, whereas the real part is with a relatively low value. As indicated in Figure 10, the loss tangent of the east face is relatively homogeneous, and it has a much lower value than that of the west one; oppositely, the west face is much more heterogeneous, especially the area on the left side. This high loss tangent of the left side on the west face should be thought of as the synergistic result of a high density of pore aqueous solutions and cracks. The photos in Figure 1 also show a high density of cracks in the left side of the west face.

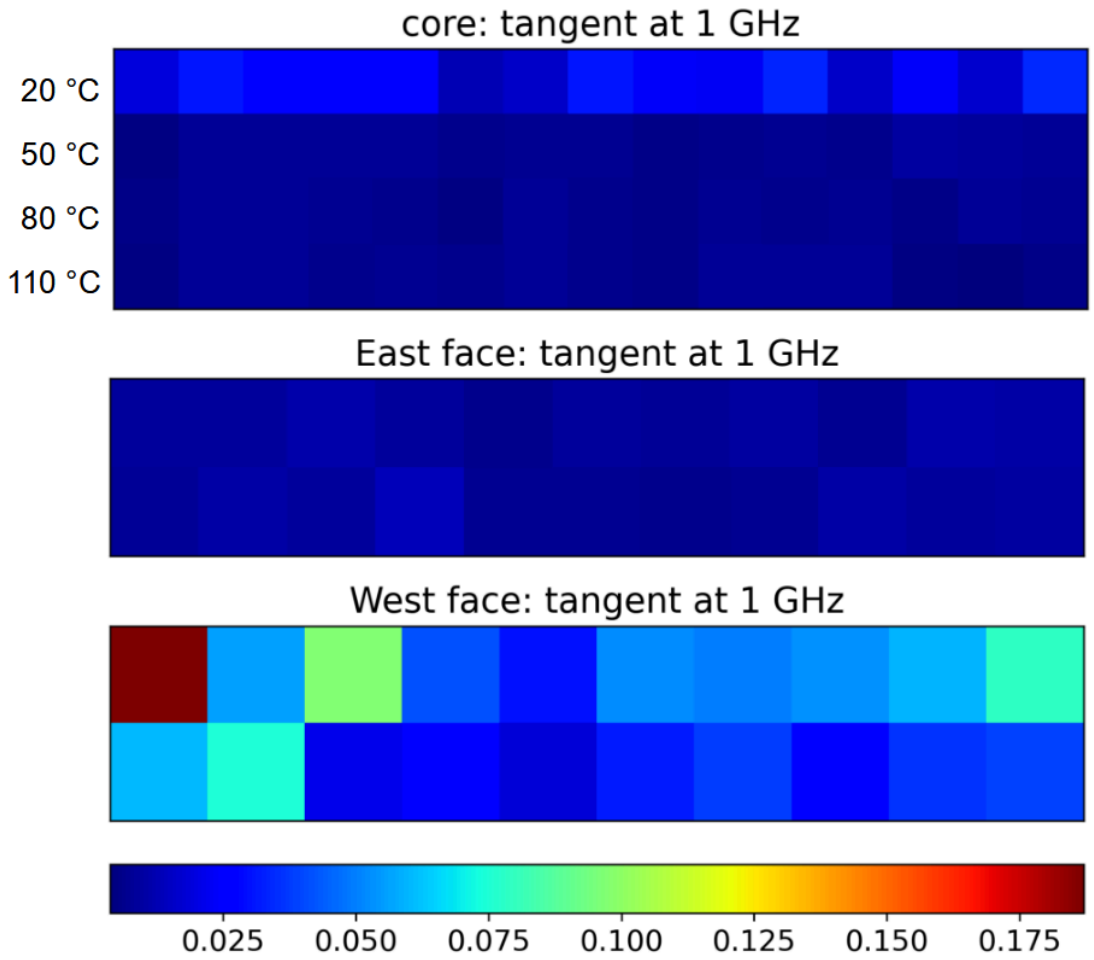

Figure 10 Loss tangent fitted at 1 GHz based on the tested results along the tested lines of the east and west faces

Conclusions

We have studied the complex permittivity of RC in a bridge's pillar by two ways: a non-destructive open-ended probe from 1 MHz to 400 MHz in an on-site investigation, and an impedance analysis from 1 Hz to 10^6 Hz for the core samples with different water contents in the laboratory. The tested complex permittivities in the two frequency domains can be related by a board band polarization mechanism based on α and β polarizations. Then the obtained fitted complex permittivity at 1 GHz can help to distinguish the influences of the water from the aqueous pore solution in the RC. By comparing the different levels of loss tangent of the points on the bridge, we can map the concrete with a high density of aqueous pore solution, which helps to estimate the unhealthy area with partial damage in the bridge by an effective and non-destructive diagnosis.

Currently, in this study, we focus our discussion on the permittivity analysis in a large frequency domain, which is mainly oriented to the materials properties. As indicated, the concrete materials in the west and east faces have different loss tangent, which will change the propagation of GPR signals. In the future, we will try to study the evolutions in signal's spectrums caused by the heterogeneity due to the pathologies in the concrete. To achieve this, C-scans obtained by a 3D radar will be especially useful for "seeing" the geometry of the inner structure in the RC. In addition, other measurements like electrochemical potential mapping will also be applied to enrich our knowledge.

Acknowledgement

This work has been supported Scientific resourcing of Clim'adapt – 2022 edition, Pôle institut Carnot Clim'adapt, Cerema, France. Meanwhile, the authors are grateful to Mr. Hervé Davias and Mr. Clément Coulais for communicating with the site, and to Mr. Frédéric Le Brun for slicing the core samples.

References

[1] Hover K.C. The influence of water on the performance of concrete. Constr Build Mater. 2011; 25:3003-3013. doi: 10.1016/j.conbuildmat.2011.01.010

[2] Rodrigues R., Gaboreau S., Gance J., Ignatiadis I., Betelu S., Reinforced concrete structures: A review of corrosion mechanisms and advances in electrical methods for corrosion monitoring. Constr Build Mater. 2021; 269: 121240 doi: 10.1016/j.conbuildmat.2020.121240

[3] Figueira R.B., Sousa R., Coelho L., Azenha M., De Almeida J.M., Jorge P.A.S., Silva C.J.R., Alkali-silica reaction in concrete: Mechanisms, mitigation and test methods. Constr Build Mater. 2019; 222: 903-931, doi: 10.1016/j.conbuildmat.2019.07.230

[4] Revil A. Effective conductivity and permittivity of unsaturated porous materials in the frequency range 1mHz-1GHz, Water Resour. Res. 2013; 49: 306-327, doi:10.1029/2012WR012700

[5] Hong S., Wiggenhauser H., Helmerich R., Dong B., Dong P., Xing F. Long-term monitoring of reinforcement corrosion in concrete using ground penetrating radar, Corros. Sci. 2017; 114: 123-132. doi: 10.1016/j.corsci.2016.11.003

[6] El Hafiane Y., Smith A., Bonnet J.P., Abélard P., Blanchart P., Electrical characterization of aluminous cement at the early age in the 10 Hz-1 GHz frequency range. Cem. Concr. Res. 2000; 7:1057-1062. doi: 10.1016/S0008-8846(00)00285-4

[7] Klysz G., Balayssac J.P., Determination of volumetric water content of concrete using ground-penetrating radar, Cem. Concr. Res., 2007; 37: 1164-1171, doi: 10.1016/j.cemconres.2007.04.010

[8] Leucci G. Ground Penetrating Radar: an Application to Estimate Volumetric Water Content and Reinforced Bar Diameter in Concrete Structures. J. Adv. Concr. Technol. 2012; 10:411-422, doi: doi.org/10.3151/jact.10.411

[9] Chen W., Shen P.L., Shui Z.H. Determination of water content in fresh concrete mix based on relative dielectric constant measurement, Constr Build Mater. 2012; 34: 306-312, doi:10.1016/j.conbuildmat.2012.02.073

[10] Bastidas-Arteaga E., Schoefs F. Stochastic improvement of inspection and maintenance of corroding reinforced concrete structures placed in unsaturated environments, Eng. Struct. 2012, 41:50–62. doi: 10.1016/j.engstruct.2012.03.011

[11] Wang Y., Oleiwi H., Wang C.Y., Xiang N., Geng J. The characterization of chloride effect on concrete water sorption and its application in the modeling of concrete conditions in tidal zones, Constr Build Mater. 2020; 253: 19074. doi: 10.1016/j.conbuildmat.2020.119074

[12] Dérobert X., Villain G., Cortas R., and Chazelas, J. EM characterization of hydraulic concretes in the GPR frequency-band using a quadratic experimental design. 7th International Symposium on Nondestructive Testing in Civil Engineering, 30 June - 3 July 2009, Nantes, France .

[13] Villain G., Ihamouten A., Dérobert X., Determination of concrete water content by coupling electromagnetic mùethods: Coaxial/cylindrical transition line with capacitive probes NDT E Int. 2017; 88: 59-70, doi: 10.1016/j.ndteint.2017.02.004

[14] Dérobert X., Iaquinta J., Klysz G., Balayssac J.P., Use of capacitive and GPR techniques for the non-destructive evaluation of cover concrete. NDT E Int. 2008; 41: 44-52, doi: https://doi.org/10.1016/j.ndteint.2007.06.004

[15] Fares M., Fargier Y., Villain G., Dérobert X., Palma Lopes S., Determining the permittivity profile inside reinforced concrete using capacitive probes, NDT E Int. 2016; 79: 150-161, doi: https://doi.org/10.1016/j.ndteint.2016.01.002

[16] Filali B., Boone F., Rhazi J., Ballivy G. Design and calibration of a large open-ended coaxial probe for the measurement of the dielectric properties of concrete. IEEE Trans. Microw. Theory Techn. 2008; 10: 2322 - 2328. doi: 10.1109/TMTT.2008.2003520

[17] Grant J.P, Clarke R.N., Symm G.T. and Spyrou N.M. A critical study of the open-ended coaxial line sensor technique for RF and microwave complex permittivity measurements. J. Phys. E: Sci. Instrum. 1989; 22: 757. doi: 10.1088/0022-3735/22/9/015

[18] Guihard V., Taillade F., Balayssac J., Steck B., Sanahuja J., Deby F. Permittivity measurement of cementitious materials with an open-ended coaxial probe. Constr. Build. Mater. 2020; 230: 116946. doi: 10.1016/j.conbuildmat.2019.116946

[19] Bourdi T., Rhazi J. E., Boone F., Ballivy G. Application of Jonscher model for the characterization of the dielectric permittivity of concrete. J. Phys. D Appl. Phys. 2008; 41: 205410. doi:10.1088/0022-3727/41/20/205410

[20] Heifetz A., Bakhtiari S., Lu J., Aranson I.S., Vinokur V.M., and Bentivegna A.F. Development of microwave and impedance spectroscopy methods for in-situ nondestructive evaluation of alkali silica reaction in concrete, 2017; AIP Conference Proceedings 1806, 120003. doi: 0.1063/1.4974708

[21] Wagner N., Bore T., Robinet J.C., Coelho D., Taillade F., Delepine-Lesoille S. Dielectric relaxation behavior of callovo-oxfordian clay rock: a hydraulic-mechanical-electromagnetic coupling approach. J. Geophys. Res. Solid Earth 2013; 118: 4729-4744. doi: 10.1002/jgrb.50343

[22] Otto G.P. and Chew W.C. Improved Calibration of a large open-ended coaxial probe for dielectric measurements. IEEE Trans. Instrum. Meas. 1991; 40: 742 – 746. doi: 10.1109/19.85345

[23] Fan B., Bosc F., Liu Y., Fauchard C. Dielectric Measurement by Open-ended Coaxial Probe for Hot-Mix Asphalt Roads: from laboratory test to on-site investigation, NDT E Int., 2023; 138: 102872. doi:10.1016/j.ndteint.2023.102872

[24] Sarin P., Snoeyink V.L., Lytle D.A., Kriven W.M. Iron corrosion scales: model for scale growth, iron release and colored water formation. J. Environ. Eng. 2004; 130: 364-373. doi: 10.1061/(ASCE)0733-9372(2004)130:4(364)

[25] Kim S., Surek J., and Baker-Jarvis J. Electromagnetic Metrology on Concrete and Corrosion. J. Res. Natl. Inst. Stand. Technol. 2011; 116: 655-669. doi: 10.6028/jres.116.011

[26] Villain G., Platret G., Thiery M., Lett J., Belin P., Routhe L., Bouteloup J.F., Etude de la durabilité de la structure en béton du tablier du pont de Cheviré. Établissement public à caractère scientifique et technique. 2006; 13H 023 41

[27] Wang S. Zhang J. Gharbi O. Vivier V. Gao M. Orazem M.E., electrochemical impedance spectroscopy. Nat. Rev. Methods Primers. 2021; 1, 41. doi:10.1038/s43586-021-00039-w

[28] Andrade C., Blanco V.M., Collazo A. , Keddam M. , Novoa. X.R., Takenouti H. Cement paste hardening process studied by impedance spectroscopy. Electrochim. Acta 1999; 44: 4313-4318. doi: 10.1016/S0013-4686(99)00147-4

[29] Hashemi A., Kurtis K.E., Donnell K.M., Zoughi R. Empirical Multiphase Dielectric Mixing Model for Cement-Based Materials Containing Alkali-Silica Reaction (ASR) Gel. IEEE Trans. Instrum. Meas. 2017; 17135990: 2428 - 2436. doi: 10.1109/TIM.2017.2707927

[30] Topp G.C., Davis J.L., Annan A.P. Electromagnetic determination of soil water content: measurements in coaxial transmission lines. Water Resour. Res. 1980; 16: 574-582. doi: 10.1029/WR016i003p00574

[31] Kaatze U. Measuring the dielectric properties of materials. Ninety-year development from low-frequency techniques to broadband spectroscopy and high-frequency imaging. Meas Sci Technol. 2013; 24. 012005. doi: 10.1088/0957-0233/24/1/012005

Supporting information

Table 1 Results of GDR fitting for the core sample

piece	after thermal treatment	MSE_{real}	$MSE_{imaginary}$	ε_∞	τ_α (s)	τ_β (μs)	σ_{DC}
#1	20°C	0.2	0.04	7.35	199	4	11618
	50°C	0.02	0.02	5.84	350	141	4230
	80°C	0	0	5.12	791	548	632
	110°C	0	0	5.05	98	65	668
#2	20°C	0.3	0.04	5.29	1013	15	3098
	50°C	0.02	0.004	5.46	357	189	4430
	80°C	0.003	0	4.79	838	913	521
	110°C	0.003	0	4.68	18	77	138
#3	20°C	0.08	0.008	6	230	24	4532
	50°C	0.02	0.005	5.55	330	283	5010
	80°C	0.003	0	4.83	818	460	568
	110°C	0.002	0	4.75	787	409	423
#4	20°C	0.09	0.02	5.93	233	16	4772
	50°C	0.04	0.005	5.41	423	128	4284
	80°C	0.007	0	5.01	826	569	920
	110°C	0.001	0	4.68	790	440	266

#5	20°C	0.004	0.004	5.66	845	10	2306
	50°C	0.03	0.004	5.4	377	204	3788
	80°C	0.001	0	4.65	807	429	327
	110°C	0.002	0.001	4.71	19	19	102
#6	20°C	0.6	0.2	6	91	7	936
	50°C	0.03	0.008	5.55	373	193	2793
	80°C	0.006	0.001	5.08	107	492	894
	110°C	0.001	0	4.79	787	407	857
#7	20°C	0.4	0.2	6.58	100	8	1558
	50°C	0.02	0.005	5.54	413	126	4228
	80°C	0.007	0	4.94	798	306	773
	110°C	0.004	0.001	4.39	17	18	199
#8	20°C	0.9	0.3	5.07	282	11	3323
	50°C	0.03	0.006	5.35	378	196	2067
	80°C	0.003	0	4.82	835	413	861
	110°C	0	0	4.56	804	396	234
#9	20°C	0.2	0.06	6.44	266	9	6294
	50°C	0.06	0.02	5.66	200	163	2127
	80°C	0.004	0	5.01	859	439	1230
	110°C	0.001	0	4.74	807	309	1000

#10	20°C	0.7	0.3	5.94	190	4	2443
	50°C	0.06	0.009	5.46	372	188	2858
	80°C	0.008	0	5.01	247	481	1159
	110°C	0.006	0	4.83	846	480	1307
#11	20°C	0.1	0.03	5.62	261	16	7361
	50°C	0.04	0.007	5.49	344	190	5209
	80°C	0.001	0	4.73	844	906	827
	110°C	0.001	0	4.69	821	3175	1193
#12	20°C	0.02	0.02	6.82	250	8	12041
	50°C	0.04	0.008	5.34	423	127	846
	80°C	0.003	0	4.72	244	552	359
	110°C	0.002	0	4.6	833	580	429
#13	20°C	0.02	0.01	6.43	186	6	7099
	50°C	0.02	0.003	5.27	552	116	8869
	80°C	0.008	0.001	5.08	192	273	3501
	110°C	0.003	0	4.88	144	190	1779
#14	20°C	0.3	0.06	6.22	645	3	11037
	50°C	0.005	0.003	4.94	343	302	858
	80°C	0	0	4.64	803	294	1198
	110°C	0.01	0.003	4.62	56	95	478

#15	20°C	0.008	0.006	5.34	969	5	5019
	50°C	0.03	0.005	5.18	395	161	1494
	80°C	0.001	0	4.74	236.41	470	816
	110°C	0.001	0	4.68	771.46	393	1444

Table 2 Results of GDR fitting for the east face

Points	MSE_{real}	$MSE_{imaginary}$	ε_∞	τ_α (ns)	τ_β (ns)	σ_{DC}
Line1_P1	0.03	0.04	5.08	1486	19	0.29
Line1_P2	0.02	0.04	4.82	1512	22	0.27
Line1_P3	0.02	0.03	4.94	1681	58	0.34
Line1_P4	0.02	0.04	4.78	1508	26	0.26
Line1_P5	0.02	0.03	4.03	1469	50	0.15
Line1_P6	0.03	0.05	4.88	1453	36	0.27
Line1_P7	0.02	0.03	4.1	1139	24	0.2
Line1_P8	0.03	0.05	4.88	1518	21	0.29
Line1_P9	0.03	0.03	4.73	1486	69	0.21
Line1_P10	0.02	0.03	4.82	1680	58	0.35
Line1_P11	0.03	0.05	4.94	1519	21	0.33
Line2_P1	0.02	0.04	4.73	1407	15	0.23

Line2_P2	0.02	0.04	5.17	1582	172	0.34
Line2_P3	0.02	0.04	4.89	1515	22	0.27
Line2_P4	0.004	0.005	4.26	1404	1	0.36
Line2_P5	0.02	0.04	4.72	756	125	0.2
Line2_P6	0.02	0.04	4.37	1460	39	0.19
Line2_P7	0.02	0.04	4.35	1494	89	0.18
Line2_P8	0.03	0.05	4.78	779	132	0.21
Line2_P9	0.02	0.03	4.85	1604	88	0.31
Line2_P10	0.02	0.03	4.7	1507	17	0.27
Line2_P11	0.03	0.04	4.66	1500	20	0.28

Table 3 Results of GDR fitting for the west face

Points	MSE_{real}	$MSE_{imaginary}$	ε_∞	τ_α (ns)	τ_β (ns)	σ_{DC}
Line1_P1	0.03	0.02	4.87	546	11	0.49
Line1_P2	0.1	0.2	6.12	2277	113	2.15
Line1_P3	0.08	0.3	8.68	2651	110	5.31
Line1_P4	0.09	0.09	5.33	2080	110	1.4
Line1_P5	0.02	0.02	4.29	2253	111	0.81
Line1_P6	0.09	0.1	6.38	2187	112	2.1

Line1_P7	0.09	0.09	7.09	2198	112	2.23
Line1_P8	0.09	0.1	6.93	2193	111	2.31
Line1_P9	0.1	0.1	7.21	2289	113	2.68
Line1_P10	0.2	0.3	8.02	2185	110	3.96
Line2_P1	0.2	0.2	6.47	2373	114	2.46
Line2_P2	0.08	0.2	6.84	2532	113	3.22
Line2_P3	0.02	0.005	3.41	2154	119	0.46
Line2_P4	0.02	0.02	4.61	1940	146	0.81
Line2_P5	0.004	0.005	2.71	2124	105	0.32
Line2_P6	0.03	0.03	5.09	1917	124	1.03
Line2_P7	0.003	0.005	4.46	1777	10	1.07
Line2_P8	0.02	0.02	4.88	1866	479	0.83
Line2_P9	0.04	0.02	5.59	2323	112	1.27
Line2_P10	0.05	0.04	5.89	2185	110	1.46